Check for updates

Geophysical Research Letters

RESEARCH LETTER
10.1029/2023GL102956

The Inner Structure of STEVE-Linked SAID

Evgeny V. Mishin[1] and **Anatoly V. Streltsov**[2]

[1]Space Vehicles Directorate, Air Force Research Laboratory, Albuquerque, NM, USA, [2]Department of Physical Sciences, Embry-Riddle Aeronautical University, Daytona Beach, FL, USA

Key Points:

- Swarm satellite observations reveal the inner electromagnetic structure of STEVE-linked subauroral ion drifts (SAID)
- Ionospheric feedback instability (IFI) simulation reproduces the observed structure
- The generated nonlinear Alfvénic system coupled with the parallel electric fields makes the inner structure of STEVE and Picket Fence

Correspondence to:
E. V. Mishin,
evgeny.mishin@spaceforce.mil

Citation:
Mishin, E. V., & Streltsov, A. V. (2023). The inner structure of STEVE-linked SAID. *Geophysical Research Letters*, *50*, e2023GL102956. https://doi.org/10.1029/2023GL102956

Received 19 JAN 2023
Accepted 5 APR 2023

Abstract We found the inner electromagnetic structure of subauroral ion drifts (SAID) in the SAID-STEVE events documented by the Swarm spacecraft and numerically simulated the ionospheric feedback instability (IFI) development for one of the four similar events. Good quantitative agreement of the modeling results with the observed features shows that the ionospheric feedback mechanism captures their basic underlying physics. Simulations require nonlinear saturation of the IFI-generated dispersive Alfvén waves. That is, a strong driving field of STEVE-linked SAID with a deep density trough leads to a nonlinear system of dispersive Alfvén waves coupled with the density perturbation and parallel electric fields. As shown earlier, these fields produce the suprathermal electron population and energy balance necessary for the STEVE and Picket Fence radiation. Therefore, our results predict their inner structure.

Plain Language Summary Interpretation of subauroral arcs—STEVE and Picket Fence—inside fast subauroral flows (SAID) with depleted density and high electron temperature requires specific local distributions of ionospheric electrons and vibrationally excited neutrals. It was earlier shown that the ionospheric feedback instability in STEVE-linked SAID could provide the required features. The resulted meridional structure was not explored further, though it is essential for validation of the feedback mechanism. We discovered the inner electromagnetic structure of four similar, well-documented SAID-STEVE events from the Swarm spacecraft and numerically simulated the IFI development for one of these. Good quantitative agreement between the simulated and observed structures shows that the ionospheric feedback mechanism captures the basic underlying physics. Therefore, our results predict the inner structure of STEVE and Picket Fence.

1. Introduction

The disturbed subauroral convection in the premidnight sector is dominated by fast, $|\mathbf{V}_W| = |\mathbf{E}_\Lambda \times \mathbf{b}_0|/B_0 \geq 1$ km/s, westward flows of the width $\Delta_S \leq 100$ km in latitude, equatorward of diffuse aurora. These are known as "polarization jets" (Galperin et al., 1974) and "subauroral ion drifts" (Spiro et al., 1979). High speed, $V_W \gtrsim 4$ km/s or $E_\Lambda \gtrsim 150$–200 mV/m, SAID channels with deep troughs, $n_e \leq 10^4$ cm^{-3}, and elevated electron temperatures, $T_e \geq 5{,}000$ K, in the top ionosphere display a subset of subauroral arcs—STEVE and Picket Fence (e.g., Archer et al., 2019; Gallardo-Lacourt et al., 2018; MacDonald et al., 2018; Nishimura et al., 2019). Their spectra are radically different from usual aurora (Gillies et al., 2019) and indicate a local source of low energy, $\varepsilon < 18.75$ eV, suprathermal electrons (Mende et al., 2019; Mende & Turner, 2019) and vibrational and electronic excitation of neutral gas below ~270 km (Mishin & Streltsov, 2019; henceforth, MS2019; Harding et al., 2020). We stress that this inference is not applied to SAR arcs (e.g., Inaba et al., 2020; Martinis et al., 2022) that require the different consideration (e.g., MS2019).

MS2019 invoked the ionospheric feedback instability (IFI) instrumental in describing discrete aurora (e.g., Streltsov et al., 2012) and subauroral ULF wave structures—SAPSWS (Streltsov & Mishin, 2003, 2018, 2020, 2022; hereafter SM2003; SM2018; SM2020; SM2022). MS2019 employed a 3D model (Jia & Streltsov, 2014) with the Hall term, $\mathbf{j}_H = \Sigma_H \mathbf{E} \times \mathbf{B}$. In a 2D system ($\Sigma_\mathrm{H} = 0$), east-west-aligned "sheets" of upward and downward field-aligned currents (FACs) carried by dispersive Alfvén waves are closed by the meridional Pedersen current, $\mathbf{j}_P = \Sigma_P \mathbf{E}_\Lambda$. The resulting east-west-aligned strips have the characteristic meridional scale length about the most unstable wavelength. The Hall term rotates the developing small-scale currents and electric fields, thereby transforming the "strips" into a chain of vortices like a series of "pickets" (MS2019, Figure 3).

Mishin and Streltsov (2022; henceforth, MS2022) simulated the IFI development taking a poleward trapezoidal field of E_0 =50, 100, and 150 mV/m and assuming a plasma density depletion of $n_e^{(v)} \sim 10^3$ cm^{-3} between

© 2023 The Authors. This article has been contributed to by U.S. Government employees and their work is in the public domain in the USA.
This is an open access article under the terms of the Creative Commons Attribution-NonCommercial License, which permits use, distribution and reproduction in any medium, provided the original work is properly cited and is not used for commercial purposes.

19448007, 2023, 8, Downloaded from https://agupubs.onlinelibrary.wiley.com/doi/10.1029/2023GL102956, Wiley Online Library on [25/04/2023]. See the Terms and Conditions (https://onlinelibrary.wiley.com/terms-and-conditions) on Wiley Online Library for rules of use; OA articles are governed by the applicable Creative Commons License

≥120 and ≤200 km—a so-called ionospheric "valley" (Titheridge, 2003). In this setup, the IFI creates greatly enhanced, small-scale FACs with parallel electric fields, $E_{\parallel}$, nonlinearly increasing with E_0, and the density depletion below the F_2 peak. With these fields, an explicit solution of the Boltzmann kinetic equation gives the electron distribution function (EDF) and the power going to excitation and ionization of neutral species (the energy balance) in good quantitative agreement with that needed for Picket Fence emissions between 120 and 140 km. The theory predictions are also consistent with the STEVE emissions above 200 km.

MS2022 noted the meridional structure of STEVE resulted from the IFI but did not pursue that further. However, confirming the meridional structure of strong SAID conjugate to (long-lasting) STEVE is essential for corroboration of the feedback mechanism. Besides, Sinevich et al. (2021, 2022) reported on SAID-associated density irregularities with the same spectral index as in SAPSWS events—the cause of stormtime midlatitude scintillations (Mishin & Blaunstein, 2008; Nishimura et al., 2021). Therefore, investigating the SAID inner structure is also essential for the understanding of midlatitude scintillations.

The purpose of this paper is twofold. First, we reveal the inner structure of SAID from the electromagnetic field and plasma data measured by the Swarm spacecraft over the STEVE arc in four similar, well-documented SAID/STEVE events (Section 2). Next, the IFI development for MacDonald et al.'s (2018) STEVE event on 25 July 2016 is numerically simulated in Section 3. The explored events show a distinctive electromagnetic structure in good quantitative agreement with the ionospheric feedback mechanism. Section 4 discusses the implication of the experimental and modeling results. The main inference is that the combination of a strong driving field and depleted density profile characteristic of strong SAID leads to a nonlinear system of dispersive Alfvén waves coupled with parallel electric fields. As these fields produce the suprathermal electron population and energy balance necessary for the radiation of STEVE and Picket Fence (MS2022), our results predict their inner structure.

2. Swarm Observations

For analyses of the spatial structure, we selected four SAID events from the Swarm spacecraft in which the magnetic footprints of Swarm passed over STEVE identified in optical measurements (Archer et al., 2019; Nishimura et al., 2019). We use Swarm 16-Hz flow (electric field) from the thermal ion imager cross-track data set and 50-Hz magnetic fields, as well as 2-Hz electron density and temperature from the Langmuir probe (LP) data set (see Jørgensen et al., 2008; Knudsen et al., 2017). Figure 1 shows the selected events. Their mean characteristics are typical of the STEVE-related SAID channels. The new result is the meridional structure comprising small-scale FACs, $j_{\parallel}$, and oscillations in the electric field, δE, and flow, $\delta V \sim \delta E/B_0$ (not shown). Low-resolution LP data do not allow exploring the density trough structure (Sinevich et al., 2021, 2022).

Electric-field oscillations are obtained as $\delta E = E_{\Lambda} - <E_{\Lambda}>$, where E_{Λ} ($<E_{\Lambda}>$) stands for the raw data (data averaged over 0.5 s). To calculate small-scale FACs, we isolate the SAID-related magnetic structure, $\delta B_j = B_j - \tilde{\Delta} B_j$. Here, $\tilde{\Delta} B_j$ is the fit of the 2-s averages of magnetic components, B_j, obtained by a standard spline/pchip procedure near a small-scale channel (e.g., Mishin, 2013, Figure 6). Notably, antisymmetric δB_{East} and δB_{North} variations indicate that the satellite crossed a current sheet at an angle $\alpha \approx \arctan\left(\frac{\delta B_E}{\delta B_N}\right) \approx 45°$. The FAC's intensity in the thin current sheet approximation at $\alpha < 60°$ is given by (e.g., Rich et al., 1980; Rother et al., 2007)

$$j_{\parallel}\left[\frac{\mu A}{m^2}\right] \approx \frac{0.75}{v_{sat}\cos\alpha}\frac{\partial}{\partial t}\delta B_E \approx \frac{0.1}{\cos\alpha}\frac{\partial}{\partial t}\delta B_E \quad (1)$$

Here, δB_E (eastward) is in nT, time t in s; and $v_{sat} = 7.5$ km/s is the satellite speed.

In the selected events, $\alpha \leq 45°$, the small-scale current system comprises a series of paired, antiparallel FACs of ±10–20 μA/m^2 intensities. The FACs correlate with ±20–40 mV/m electric oscillations, δE, like in SAPSWS (e.g., Mishin et al., 2003, Figure 6). The revealed spatial variability is consistent with the small-scale FAC structure generated by the IFI inside SAID (MS2019; MS2022). Next, we show that the IFI simulation practically reproduces the satellite measurements for the 25 July 2016 event.

3. Simulation of the 25 July 2016 Event

The IFI develops as short transverse-wavelength, $\lambda_{A\perp} \sim$ 1–10 km, dispersive Alfvén waves are "over-reflected" from the E-region ionosphere with a strongly sheared convection flow due to the altitude-dependent ion-neutral

19448007, 2023, 8, Downloaded from https://agupubs.onlinelibrary.wiley.com/doi/10.1029/2023GL102956, Wiley Online Library on [25/04/2023]. See the Terms and Conditions (https://onlinelibrary.wiley.com/terms-and-conditions) on Wiley Online Library for rules of use; OA articles are governed by the applicable Creative Commons License

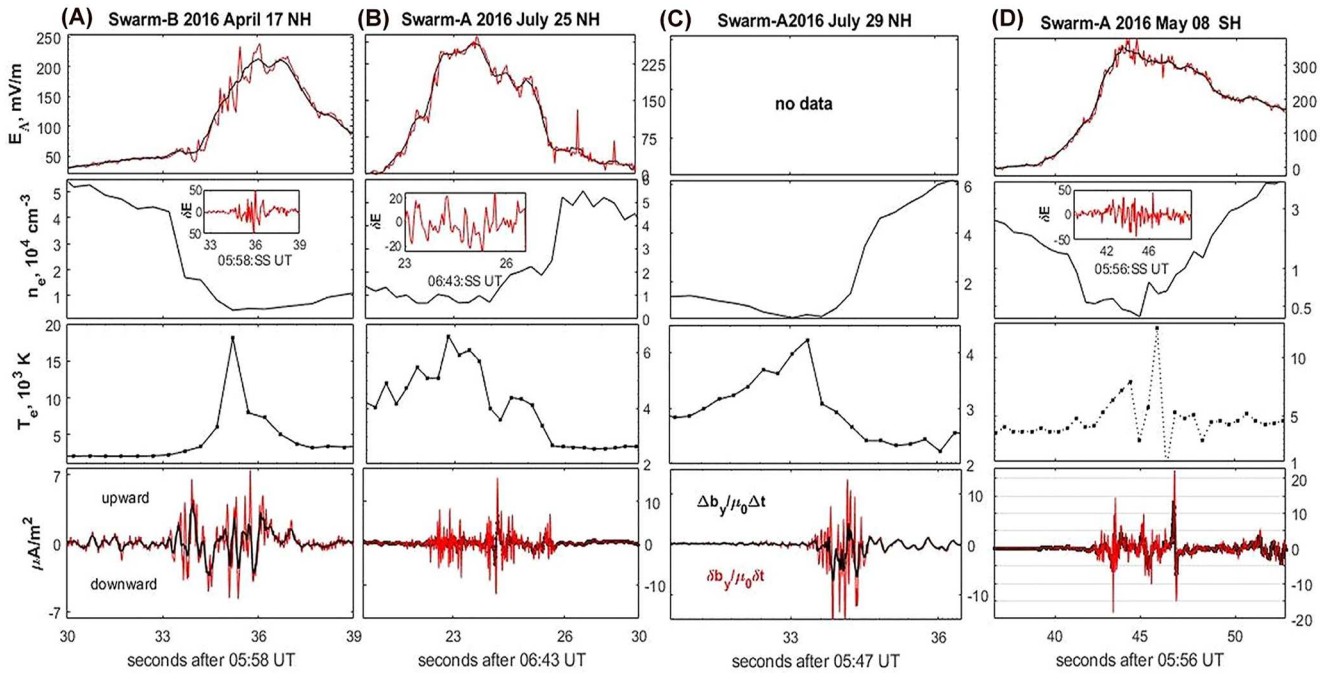

Figure 1. Four SAID-STEVE events. (Top row): Meridional electric fields. Red (black) curves show the raw data, E_Λ (data averaged over 0.5 s, $<E_\Lambda>$); second and third: The plasma density and electron temperature. Insets: Electric-field oscillations, $\delta E = E_\Lambda - <E_\Lambda>$. Bottom: Small-scale field-aligned currents, $j_\parallel$. Red (black) curves show field-aligned currents (FACs) calculated from δB_E averaged over 0.3 s (0.8 s).

collision frequency, $\nu_i(h)$. In general, the favorable conditions for the IFI include the presence of the large-scale electric field in the ionosphere and the low E-region plasma density of $n_{0E} \leq 10^4$ cm^{-3}. Then, the IFI threshold is quite low: $E_{th} \approx 50\Omega_{ci}/\nu_{i0} \sim$20–30 mV/m (Trakhtengertz & Feldstein, 1991). Here, $\nu_{i0} = \nu_i(h_0)$ and Ω_{ci} is the ion gyrofrequency at $h_0 = 110$ km. We use the reduced two-fluid MHD model (e.g., SM2003; SM2018) describing dispersive Alfvén waves in low-β plasmas.

In the magnetosphere, dispersive Alfvén waves are described by equations for the electron parallel momentum, $m_e nu$, continuity of the plasma density, n, and the current continuity equation. The ionospheric boundaries of the domain are set at h_0. The vertical size, $h \sim$ 10–15 km, of the E-region conducting (dynamo) layer is much less than $\lambda_{A\parallel} \sim 10^3$ km, so the plasma density and electric field in the layer can be taken uniform. Integrating the current continuity equation, $\nabla \cdot \mathbf{j} = 0$, over the dynamo layer gives the simplest (so-called electrostatic) boundary conditions in the E-region.

$$\nabla \cdot (\Sigma_P \mathbf{E}_\perp) = \pm j_{\parallel,i} \tag{2}$$

Here, $j_{\parallel,i}$ is the FAC density on the top of the dynamo layer and the sign "$\pm$" in the right-hand side of Equation 2 is for the southern/northern hemisphere. Integrating the continuity equation over the dynamo layer yields the density variation

$$\frac{\partial n}{\partial t} + \nabla_\perp \cdot (n\mathbf{v}_E) = \frac{j_\parallel}{eh} + \alpha\left(n_0^2 - n^2\right) \tag{3}$$

Here, $\mathbf{v}_E = \mathbf{E} \times \mathbf{b}_0 / B_0$, α is the recombination coefficient; the term αn^2 represents losses due to the recombination, while αn_0^2 represents all unspecified sources of the ionospheric plasma that provide the equilibrium state of the ionosphere n_0. Note that the above equations are not linearized.

The computational domain in Figure 2 represents a 2D slice of the axisymmetric dipole magnetic field in the SAID channel across the indicated magnetic shells, L. The input (driving) electric field at the satellite altitude is the low-frequency part, $E_L(L)$ (black line in Figure 2a), obtained by applying the low-pass (0.5 Hz cutoff frequency) filter to the measured field, E_Λ (Figure 1b). Inside the whole domain, the current-free equilibrium field, $E_0(L, s)$,

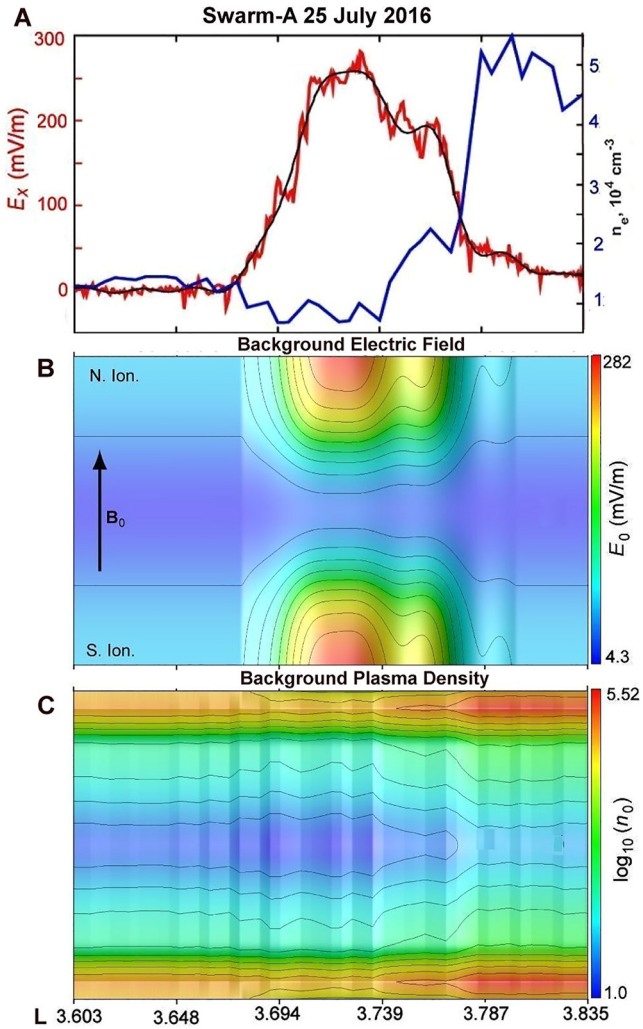

Figure 2. (a) The measured, E_Λ (red curve), electric field and the lowpass-filtered driving field, $E_L(L)$ (black) with the plasma density, $n_{01}(L)$ (blue), along the Swarm-A pass on 25 July 2016. The spatial distribution in the computational domain of (b) $E_0(L, s)$ and (c) $n_0(L, s)$ (see text).

is obtained by extending $E_L(L)$ electrostatically along the geomagnetic field between the hemispheres. Here, s is the distance along the magnetic field. Regarding the density distribution along the entire magnetic field line, over the past 20+ years of modeling the ionosphere-magnetosphere coupling we developed a robust density model from one hemisphere to another (e.g., SM2018, SM2020). The model interpolates density between the ionospheric E-region and F-region and the equatorial magnetosphere. Thus, to get the density in the entire magnetosphere, the user needs to specify the density in these three locations. The density in the equatorial magnetosphere is taken from the coincident Van Allen Probe A and B data. The density in the F-region is defined from the measurements of Swarm satellites during the event. Thus, the density inside the domain is defined as $n_0(L, s) = n_{01}(L)n_{02}(s)$ (cf. SM2018, Equation 6). Here, $n_{01}(L)$ is the measured density variation in Figure 2a and $n_{02}(s)$ is chosen to provide the minimum plasma density $n_{0E} = 10^4$ cm^{-3} at 110 km (e.g., Kelley, 2009), $n_{0F} = 6 \times 10^4$ cm^{-3} at 300 km (F_2 peak), and $n_0 = 10$ cm^{-3} in the equatorial magnetosphere.

As in MS2019 and MS2022, computations have been performed using the numerical procedure described in detail in (SM2003; 2018; 2020; 2022). Therefore, here we present only the simulation results. Simulation spans a 692 s period, starting from quiet, unperturbed conditions. The IFI was initiated by a numerical noise representing random thermal fluctuations of the plasma density. Figure 3 describes the temporal dynamics and spatial structure of the small-scale FACs in dispersive Alfvén waves and the associated meridional electric fields. As in MS2022 (Figure 2), FACs are also associated with enhanced parallel fields (not shown) responsible for the arc radiation.

Specifically, Figure 3b shows three snapshots of the simulated FACs taken at the "initial" stage, $t_1 = 207.6$ s, and at saturation, $t_2 = 415.2$ s, and $t_3 = 622.8$ s Figure 3c illustrates the simulated perpendicular electric field at the Swarm-A altitude of ≈450 km, while Figure 3d shows its relative power spectral density. Notice the change in the characteristic ULF wave frequency from ≈50 to ≈35 mHz and in the current structure at the domain's left and right flanks, like in the observed FACs (Figure 1b).

To make a detailed comparison between the simulation and the data, a virtual satellite was "launched" through the simulation domain along the Swarm-A pass. Figure 4 illustrates the Swarm-A data and "measurements" from the virtual satellite designated by the subscript "*sim*". Besides $E_L(L)$ and $n_{01}(L)$, Figure 4a shows electric field oscillations, δE_L and δE_f, obtained by applying a highpass, $f > 0.5$ Hz, and a bandpass, $0.5 < f < 2.0$ Hz, filter to the measured field, respectively. Figure 4b shows the simulated field, E_{sim}, and the plasma density, as well as the smoothed, $f \leq 0.33$ Hz, $<E_{sim}>$ and high frequency, $f > 0.33$ Hz, δE_{sim}, components.

For a direct comparison, the observed and simulated electric oscillations, δE_f and δE_{sim}, are presented in Figure 4c, while their power spectral densities (PSD) are shown in Figure 4d. For the spacecraft velocity of $V_{s,\perp} \sim 7.5$ km/s across the SAID channel, the Doppler-shifted frequencies, 0.4 and 0.6 Hz, correspond to $\lambda_\perp \sim V_{s,\perp}/f \approx 19$ and 12 km wavelengths, respectively. The different frequencies (wavelengths) come from the different patterns at the simulation domain's flanks. Evidently, not only the simulated spatial structure is very much alike the observed pattern, but also their magnitudes are close. Therefore, the numerical results demonstrate good quantitative agreement with the observations.

As shown earlier (Jia & Streltsov, 2014; MS19), the amplitudes of the IFI-generated small-scale FACs in the Picket Fence, 3D geometry with the Hall current are slightly larger than in the 2D/STEVE case. That is, for the same input conditions, simulations in a full, far more time-consuming 3D geometry would give slightly larger δE_{sim} than shown above. Therefore, the above 2D results can be qualitatively applied to Picket Fence when $\Sigma_H > \Sigma_P$.

19448007, 2023, 8, Downloaded from https://agupubs.onlinelibrary.wiley.com/doi/10.1029/2023GL102956, Wiley Online Library on [25/04/2023]. See the Terms and Conditions (https://onlinelibrary.wiley.com/terms-and-conditions) on Wiley Online Library for rules of use; OA articles are governed by the applicable Creative Commons License

19448007, 2023, 8, Downloaded from https://agupubs.onlinelibrary.wiley.com/doi/10.1029/2023GL102956, Wiley Online Library on [25/04/2023]. See the Terms and Conditions (https://onlinelibrary.wiley.com/terms-and-conditions) on Wiley Online Library for rules of use; OA articles are governed by the applicable Creative Commons License

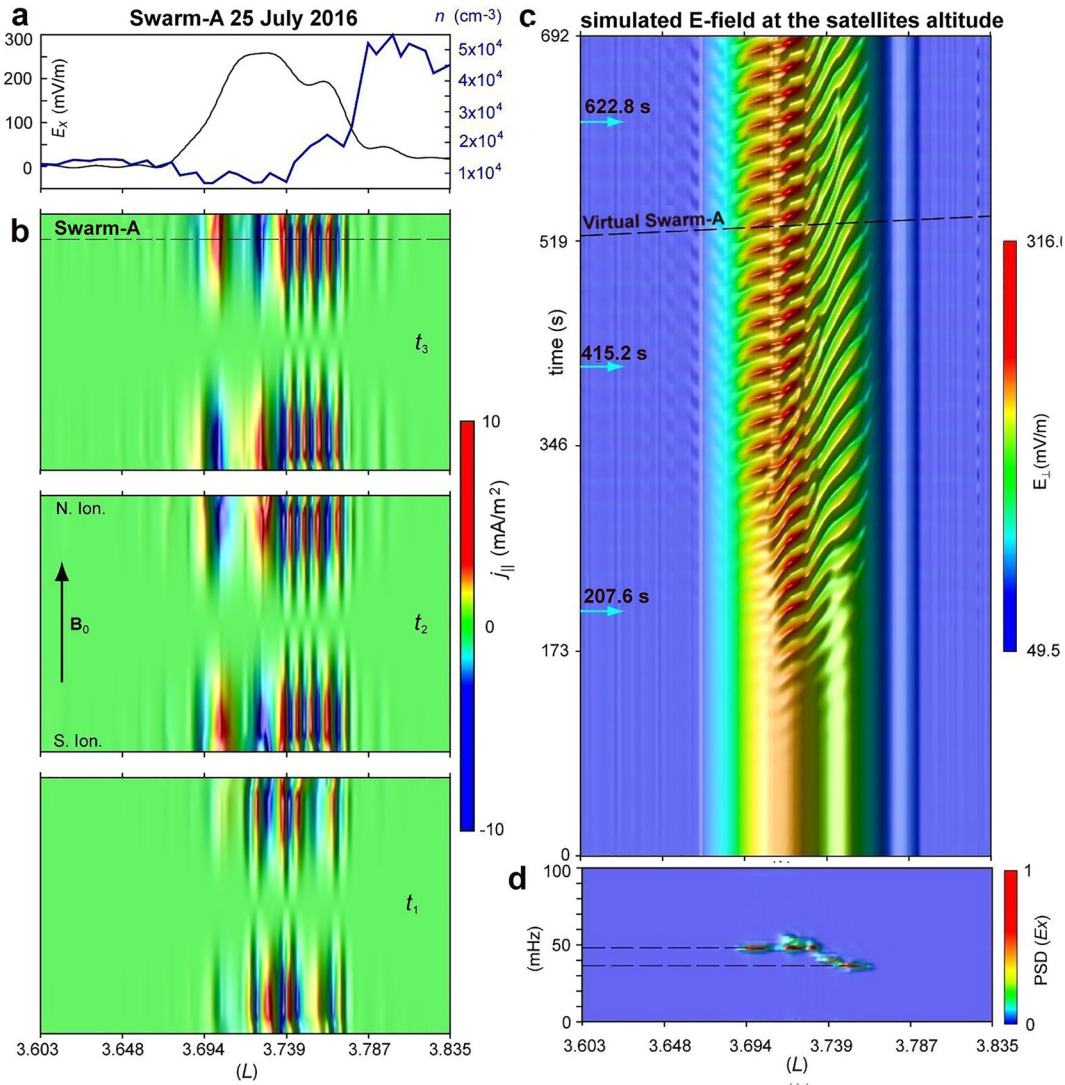

Figure 3. (a) The driving electric field, $E_L(L)$, and the plasma density, $n_{01}(L)$ (blue), along the Swarm-A pass. (b) Three snapshots of the field-aligned currents (FACs) density, $j_{\|}$, in the simulation domain at times indicated by arrows in frame c (see text). The dashed line marks the Swarm-A pass. (c) Temporal dynamics and spatial structure of the simulated transverse electric field. The dashed line marks the space-time "trajectory" of a virtual satellite. (d) Power spectral density of the ULF electric field along the virtual satellite trajectory.

4. Discussion and Conclusion

Good quantitative agreement with the observations indicates that the model describes the essence of the SAID evolution. We must note that the currents in the simulation were continuously increasing with time because the model does not include self-consistent saturation mechanisms of the IFI-generated ULF waves in the nonlinear regime. One of these in the E-region could be the electron heating due to the Farley-Buneman instability (e.g., Dimant & Milikh, 2003) that changes the recombination rate and conductivity. Additionally, there are several conceivable saturation mechanisms of the IFI-generated dispersive Alfvén waves/FACs in the top ionosphere, such as the FAC-driven ion acoustic instability. Indeed, with the obtained small-scale FACs, the electron parallel drift velocity, $u = |j_{\|}|/n_e e$, in the depleted plasma exceeds the ion sound speed. However, in the trough the excited wave spectrum is one-dimensional and the "classical" anomalous resistivity (e.g., Galeev & Sagdeev, 1984) does not apply. For the input constant parallel electric field, the instability results in the generation of intermittent ion acoustic double layers and electron heating (e.g., Chanteur et al., 1983; Sato & Okuda, 1980). In saturation, the electron current and thermal velocities linearly grow with time. Regrettably, this problem for the input current has not yet been investigated.

19448007, 2023, 8, Downloaded from https://agupubs.onlinelibrary.wiley.com/doi/10.1029/2023GL102956, Wiley Online Library on [25/04/2023]. See the Terms and Conditions (https://onlinelibrary.wiley.com/terms-and-conditions) on Wiley Online Library for rules of use; OA articles are governed by the applicable Creative Commons License

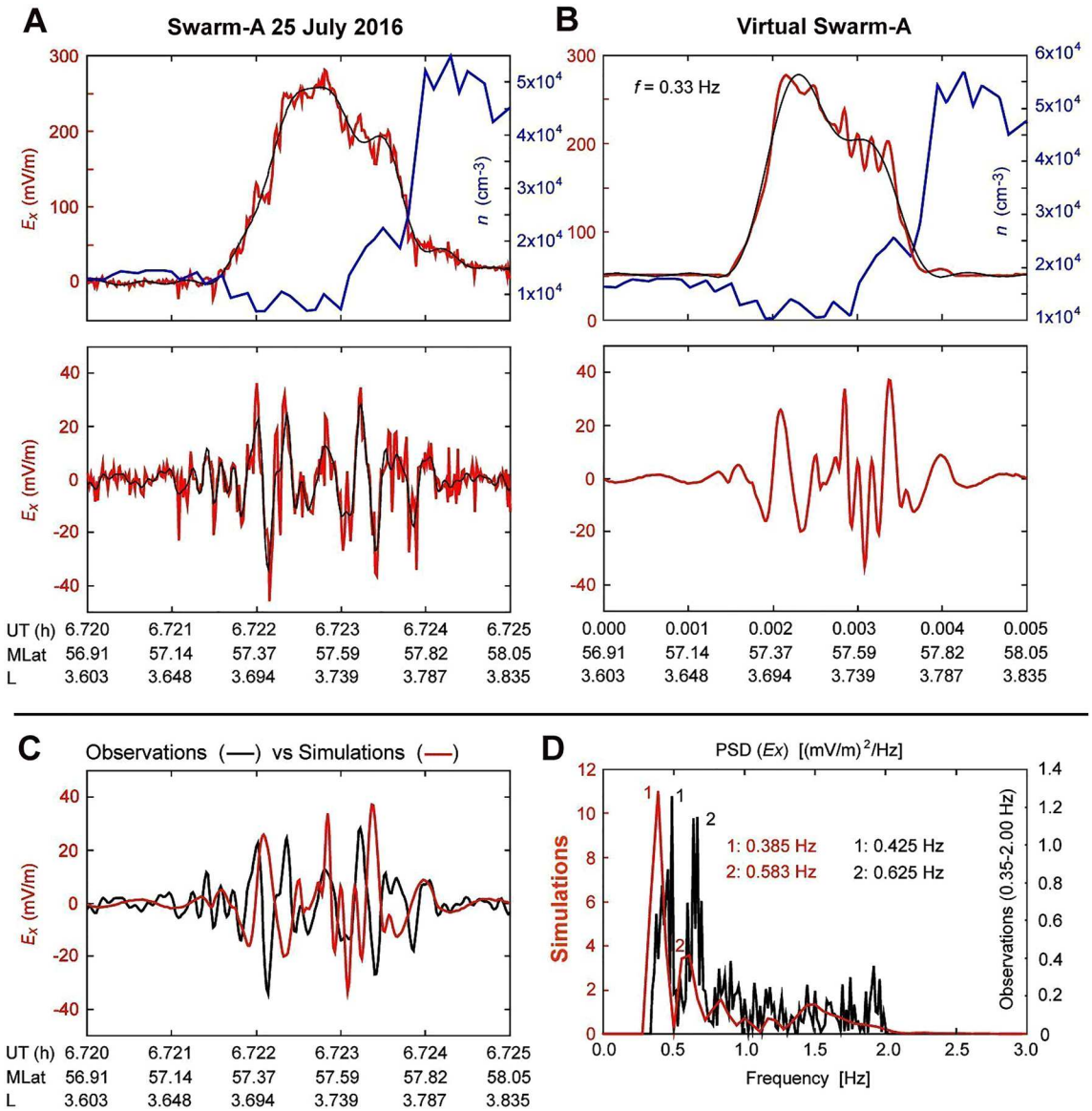

Figure 4. (a) Top: The same as Figure 2a. Bottom: Filtered electric-field oscillations: δE_L at $f > 0.5$ Hz (red) and δE_f at $0.5 < f < 2.0$ Hz (black). (b) Top: The simulated electric field (red color, E_{sim}) and its low-frequency part at $f \leq 0.33$ Hz (black, $<E_{sim}>$) with the plasma density (blue) along the virtual satellite trajectory. Bottom: Electric-field oscillations at $f > 0.33$ Hz, δE_{sim}. (c) Observed and simulated electric-field oscillations, δE_f (black) and δE_{sim} (red). (d) The power spectral density of δE (black) and δE_{sim} (red) with the peak Doppler-shifted frequencies indicated.

Mishin and Streltsov (2021, Chapter 2.3) noticed that IFI-generated Alfvén waves could be parametrically unstable and generate convective cells, that is, local small-scale vortices. For the parameters in the top ionosphere, the threshold, $\left(1 + k_\perp^2 \lambda_e^2\right)^{3/2} \delta B_{\mathbf{k}} > B_0 k_z \lambda_e q/2k$ (Pokhotelov et al., 2003; Volokitin & Dubinin, 1989), is satisfied for FACs of ~10 μA/m^2. Here, λ_e is the electron skin length, $k_z/k_\perp$ is the parallel/perpendicular to $\mathbf{B}_0$ wavevector component, and $q^{-1} > k^{-1}$ is the cell's characteristic scale size. Similarly, Lynch et al. (2022) suggested a tearing instability in intense FACs for the formation of small-scale vortices. In other words, a picket fence-like structure can be formed even without the Hall conductivity.

To allow for possible stabilization effects, we introduced a limiting threshold on the variation of the ionosphere density defined by Equation 3. Mathematically, this threshold is defined as $(1 \pm \delta_T)\, n_{0E}$, where n_{0E} is the background density in the ionospheric E-region (the ionospheric boundary of the domain), and δ_T is the number in the range from 0 to 1. Thus, if the density, n, becomes less than $(1 - \delta_T)\, n_{0E}$ or greater than $(1 + \delta_T)\, n_{0E}$, then it

19448007, 2023, 8, Downloaded from https://agupubs.onlinelibrary.wiley.com/doi/10.1029/2023GL102956, Wiley Online Library on [25/04/2023]. See the Terms and Conditions (https://onlinelibrary.wiley.com/terms-and-conditions) on Wiley Online Library for rules of use; OA articles are governed by the applicable Creative Commons License

is replaced with $(1 - \delta_T)\, n_{0E}$ or $(1 + \delta_T)\, n_{0E}$, respectively. Simulations show that the variation of δ_T changes both the magnitude and structure of the FACs.

In the above simulation, we consider that the IFI is saturated when the simulated FACs' intensities (Figure 3b) match the observed values of $j_m = \pm 10\ \mu A/m^2$ (Figure 1b). This determines the saturation threshold of $\delta_T \approx 0.2$. Then, the electric field (Figures 3c and 4b) is obtained from the artificially saturated FACs. That is, the numerical results reproduce in detail the observed electromagnetic structure when the IFI-produced density variation is limited to ±20% of the background value. The simulation-observation congruency indicates that the ionospheric feedback via ULF Alfvén waves creating a nonlinear system of dispersive Alfvén waves coupled with the density perturbations captures the basic underlying physics of the magnetosphere-ionosphere coupling in the STEVE/SAID region.

In conclusion, we revealed the inner electromagnetic structure of STEVE-associated fast SAID and performed its numerical investigation using approach based on the ionospheric feedback mechanism (MS2019; MS2022). Simulation of the IFI development for one of the observational events reproduces in detail the structure and amplitude of the observed electric fields and field-aligned currents. The important parameter used in the simulation is the saturation threshold of the instability, which defines the spatial structure and amplitude of the intense ULF waves and currents generated by the instability in a nonlinear regime. Good quantitative agreement between the observed and simulated electromagnetic patterns indicates that the model captures the basic underlying physics of the nonlinear magnetosphere-ionosphere coupling via ULF Alfvén waves in the STEVE/SAID region.

Obviously, more theoretical efforts are required to identify the saturation mechanism and its dependence on the background parameters, especially on the E-region plasma density. This formidable task is beyond the scope of this paper but we plan to perform a series of simulations to find the dependence (if any) of the electromagnetic structure and δ_T on n_{0E}. This paper was under review when Sinevich et al. (2023) reported on a stratified internal structure of the density trough inside SAID (in short, SSAID) from the NorSat-1 satellite, while Nishimura et al. (2023) showed fine-scale structures within the STEVE arc captured by citizen scientist photographs and the Transition Region Explorer imager and spectrograph observations at Lucky Lake, Canada. The SSAID pattern is similar to the electromagnetic pattern found in our work.

Data Availability Statement

The Swarm data used in this study were obtained at https://swarm-diss.eo.esa.int/#swarm/. The code used in the simulations, data files used to run the code and the results from the simulation shown in Figures 3 and 4 are available from Figshare.com https://doi.org/10.6084/m9.figshare.22232890.

Acknowledgments
E.V.M. and A.V.S. acknowledge support by the Air Force Office of Scientific Research LRIR 22RVCOR011 and the NSF Award AGS 1803702, respectively. Approved for public release; distribution is unlimited. Public Affairs release approval #AFRL-2023-0575. The views expressed are those of the authors and do not reflect the official guidance or position of the United States Government, the Department of Defense or of the United States Air Force.

References

Archer, W., Gallardo-Lacourt, B., Perry, G., St.-Maurice, J.-P., Buchert, S., & Donovan, E. (2019). Steve: The optical signature of intense subauroral ion drifts. *Geophysical Research Letters*, *46*, 6279–6286. https://doi.org/10.1029/2019GL082687

Chanteur, G., Adam, J., Pellat, R., & Volokitin, A. (1983). Formation of ion acoustic double layers. *Physics of Fluids*, *26*(6), 1584–1586. https://doi.org/10.1063/1.864293

Dimant, Y., & Milikh, G. (2003). Model of anomalous electron heating in the E region: 1. Basic theory. *Journal of Geophysical Research*, *108*(A9), 1350. https://doi.org/10.1029/2002JA009524

Galeev, A., & Sagdeev, R. (1984). Current instabilities and anomalous resistivity of plasmas. In A. Galeev, & R. Sudan (Eds.), *Basic plasma physics* (Vol. 2, Suppl, pp. 271–335). Elsevier.

Gallardo-Lacourt, B., Liang, J., Nishimura, Y., & Donovan, E. (2018). On the origin of STEVE: Particle precipitation or ionospheric skyglow? *Geophysical Research Letters*, *45*, 7968–7973. https://doi.org/10.1029/2018GL078509

Galperin, Y., Ponomarev, V., & Zosimova, A. (1974). Plasma convection in the polar ionosphere. *Annales Geophysicae*, *30*, 1–7.

Gillies, D., Donovan, E., Hampton, D., Liang, J., Connors, M., Nishimura, Y., et al. (2019). First observations from the TREx spectrograph: The optical spectrum of STEVE and the Picket Fence phenomena. *Geophysical Research Letters*, *46*, 7207–7213. https://doi.org/10.1029/2019GL083272

Harding, B., Mende, S., Triplett, C., & Wu, Y. J. (2020). A mechanism for the STEVE continuum emission. *Geophysical Research Letters*, *47*, e2020GL087102. https://doi.org/10.1029/2020GL087102

Inaba, Y., Shiokawa, K., Oyama, S.-i., Otsuka, Y., Oksanen, A., Shinbori, A., et al. (2020). Plasma and field observations in the magnetospheric source region of a stable auroral red (SAR) arc by the Arase satellite on 28 March 2017. *Journal of Geophysical Research: Space Physics*, *125*, e2020JA028068. https://doi.org/10.1029/2020JA028068

Jia, N., & Streltsov, A. (2014). Ionospheric feedback instability and active discrete auroral forms. *Journal of Geophysical Research: Space Physics*, *119*, 2243–2254. https://doi.org/10.1002/2013JA019217

Jørgensen, J. L., Friis-Christensen, E., Brauer, P., Primdahl, F., Jørgensen, P. S., Allin, T. H., & Denver, T. (2008). *The Swarm magnetometry package*. In *Small satellites for earth observation* (pp. 143–151). Springer.

Kelley, M. C. (2009). *The Earth's ionosphere: Plasma physics and electrodynamics*. Academic Press. ISBN 978-0-12-088425-4.

Knudsen, D. J., Burchill, J. K., Buchert, S. C., Eriksson, A., Gill, R., Wahlund, J.-E., et al. (2017). Thermal ion imagers and Langmuir probes in the Swarm electric field instruments. *Journal of Geophysical Research: Space Physics*, *122*, 2655–2673. https://doi.org/10.1002/2016JA022571

Lynch, K., McManus, E., Gutow, J., Burleigh, M., & Zettergren, M. (2022). An ionospheric conductance gradient driver for subauroral picket fence visible signatures near STEVE events. *Journal of Geophysical Research: Space Physics*, *127*, e2022JA030863. https://doi.org/10.1029/2022JA030863

MacDonald, E., Donovan, E., Nishimura, Y., Case, N., Gillies, D. M., Gallardo-Lacourt, B., et al. (2018). New science in plain sight: Citizen scientists lead to the discovery of optical structure in the upper atmosphere. *Science Advances*, *4*(3), eaaq0030. https://doi.org/10.1126/sciadv.aaq0030

Martinis, C., Griffin, I., Gallardo-Lacourt, B., Wroten, J., Nishimura, Y., Baumgardner, J., & Knudsen, D. J. (2022). Rainbow of the night: First direct observation of a SAR arc evolving into STEVE. *Geophysical Research Letters*, *49*, e2022GL098511. https://doi.org/10.1029/2022GL098511

Mende, S. B., Harding, B. J., & Turner, C. (2019). Subauroral green STEVE arcs: Evidence for low-energy excitation. *Geophysical Research Letters*, *46*, 14256–14262. https://doi.org/10.1029/2019GL086145

Mende, S. B., & Turner, C. (2019). Color ratios of subauroral (STEVE) arcs. *Journal of Geophysical Research: Space Physics*, *124*, 5945–5955. https://doi.org/10.1029/2019JA026851

Mishin, E. (2013). Interaction of substorm injections with the subauroral geospace: 1. Multispacecraft observations of SAID. *Journal of Geophysical Research: Space Physics*, *118*, 5782–5796. https://doi.org/10.1002/jgra.50548

Mishin, E., & Blaunstein, N. (2008). Irregularities within subauroral polarization stream-related troughs and GPS radio interference at midlatitudes. In P. M. Kintner Jr., A. J. Coster, T. Fuller-Rowell, A. J. Mannucci, M. Mendillo, & R. Heelis (Eds.), *MidLatitude ionospheric dynamics and disturbances* (Vol. 181, pp. 291–295). Geophysical Monograph Series. https://doi.org/10.1029/181GM26

Mishin, E., Burke, W., Huang, C., & Rich, F. (2003). Electromagnetic wave structures within subauroral polarization streams. *Journal of Geophysical Research*, *108*(A8), 1309. https://doi.org/10.1029/2002JA009793

Mishin, E., & Streltsov, A. (2019). STEVE and the picket fence: Evidence of feedback-unstable magnetosphere-ionosphere interaction. *Geophysical Research Letters*, *46*, 14247–14255. https://doi.org/10.1029/2019GL085446

Mishin, E., & Streltsov, A. (2021). *Nonlinear wave and plasma structures in the auroral and subauroral geospace*. Elsevier.

Mishin, E., & Streltsov, A. (2022). On the kinetic theory of subauroral arcs. *Journal of Geophysical Research: Space Physics*, *127*, e2022JA030667. https://doi.org/10.1029/2022JA030667

Nishimura, Y., Dyer, A., Kangas, L., Donovan, E., & Angelopoulos, V. (2023). Unsolved problems in strong thermal emission velocity Enhancement (STEVE) and the picket fence. *Frontiers in Astronomy and Space Sciences*, *10*, 1087974. https://doi.org/10.3389/fspas.2023.1087974

Nishimura, Y., Gallardo-Lacourt, B., Zou, Y., Mishin, E., Knudsen, D. J., Donovan, E. F., & Raybell, R. (2019). Magnetospheric signatures of STEVE: Implications for the magnetospheric energy source and interhemispheric conjugacy. *Geophysical Research Letters*, *46*, 5637–5644. https://doi.org/10.1029/2019GL082460

Nishimura, Y., Mrak, S., Semeter, J., Coster, A., Jayachandran, P., Groves, K., et al. (2021). Evolution of mid-latitude density irregularities and scintillation in North America during the 7–8 September 2017 storm. *Journal of Geophysical Research: Space Physics*, *126*, e2021JA029192. https://doi.org/10.1029/2021JA029192

Pokhotelov, O., Onishchenko, O., Sagdeev, R., & Treumann, R. (2003). Nonlinear dynamics of inertial Alfvén waves in the upper ionosphere: Parametric generation of electrostatic convective cells. *Journal of Geophysical Research*, *108*(A7), 1291. https://doi.org/10.1029/2003JA009888$09.00

Rich, F., Burke, W., Kelley, M., & Smiddy, M. (1980). Observations of field-aligned currents in association with strong convection electric fields at subauroral latitudes. *Journal of Geophysical Research*, *85*(A5), 2335–2340. https://doi.org/10.1029/JA085ia05p02335

Rother, M., Schlegel, K., & Lühr, H. (2007). CHAMP observation of intense kilometer-scale field-aligned currents, evidence for an ionospheric Alfvén resonator. *Annales Geophysicae*, *25*(7), 1603–1615. https://doi.org/10.5194/angeo-25-1603-2007

Sato, T., & Okuda, H. (1980). Ion acoustic double layers. *Physical Review Letters*, *44*(11), 740–743. https://doi.org/10.1103/physrevlett.44.740

Sinevich, A., Chernyshov, A., Chugunin, D., Clausen, L. B. N., Miloch, W. J., & Mogilevsky, M. M. (2023). Stratified subauroral ion drift (SSAID). *Journal of Geophysical Research: Space Physics*, *128*, e2022JA031109. https://doi.org/10.1029/2022JA031109

Sinevich, A., Chernyshov, A., Chugunin, D., Miloch, W. J., & Mogilevsky, M. M. (2021). Spatial structure of polarization jet according to NorSat-1 and Swarm satellite data. *Cosmic Research*, *59*(6), 463–471. https://doi.org/10.1134/S0010952521060095

Sinevich, A., Chernyshov, A., Chugunin, D., Oinats, A. V., Clausen, L. B. N., Miloch, W. J., et al. (2022). Small-scale irregularities within polarization jet/SAID during geomagnetic activity. *Geophysical Research Letters*, *49*, e2021GL097107. https://doi.org/10.1029/2021GL097107

Spiro, R., Heelis, R., & Hanson, W. (1979). Rapid subauroral ion drifts observed by Atmosphere Explorer C. *Geophysical Research Letters*, *6*(8), 657–660. https://doi.org/10.1029/GL006i008p00657

Streltsov, A., Jia, N., Pedersen, T., Frey, H., & Donovan, E. (2012). ULF waves and discrete aurora. *Journal of Geophysical Research*, *117*, A09227. https://doi.org/10.1029/2012JA017644

Streltsov, A., & Mishin, E. (2003). Numerical modeling of localized electromagnetic waves in the nightside subauroral zone. *Journal of Geophysical Research*, *108*(A8), 1332. https://doi.org/10.1029/2003JA009858

Streltsov, A., & Mishin, E. (2018). Ultralow frequency electrodynamics of magnetosphere-ionosphere interactions near the plasmapause during substorms. *Journal of Geophysical Research: Space Physics*, *123*, 7441–7451. https://doi.org/10.1029/2018JA025899

Streltsov, A., & Mishin, E. (2020). ULF waves generated near the plasmapause by the magnetosphere-ionosphere interactions. *Journal of Geophysical Research: Space Physics*, *125*, e2019JA027353. https://doi.org/10.1029/2019JA027353

Streltsov, A., & Mishin, E. (2022). Ionospheric feedback and ULF quarter-waves. *Journal of Geophysical Research: Space Physics*, *127*, e2022JA030659. https://doi.org/10.1029/2022JA030659

Titheridge, J. (2003). Ionization below the night F2 layer—A global model. *Journal of Atmospheric and Solar-Terrestrial Physics*, *65*, 1035–1052. https://doi.org/10.1016/S1364-6826(03)00136-6

Trakhtengertz, V., & Feldstein, A. (1991). Turbulent Alfvén boundary layer in the polar ionosphere. 1. Excitation conditions and energetics. *Journal of Geophysical Research*, *96*, 19363–19374.

Volokitin, A., & Dubinin, E. (1989). The turbulence of Alfvén waves in the polar magnetosphere of the Earth. *Planetary Space Science*, *37*(7), 761–765. https://doi.org/10.1016/0032-0633(89)90127-x

19448007, 2023, 8, Downloaded from https://agupubs.onlinelibrary.wiley.com/doi/10.1029/2023GL102956, Wiley Online Library on [25/04/2023]. See the Terms and Conditions (https://onlinelibrary.wiley.com/terms-and-conditions) on Wiley Online Library for rules of use; OA articles are governed by the applicable Creative Commons License